Quaternary Geochronology 67 (2022) 101241

Contents lists available at ScienceDirect

Quaternary Geochronology

journal homepage: www.elsevier.com/locate/quageo

Luminescence dating of quartz from ironstones of the Xingu River, Eastern Amazonia

P. Niyonzima [a,*], A.O. Sawakuchi [a], D.J. Bertassoli Jr. [b], F.N. Pupim [c], N. Porat [d], M.P. Freire [a], A. M. Góes [a], F.C.G. Rodrigues [a]

[a] Institute of Geosciences, University of São Paulo, Rua do lago 562, São Paulo, SP, 05508-080, Brazil
[b] School of Arts, Sciences and Humanities, University of São Paulo, Av. Arlindo Bettio, 1000, São Paulo, SP, 03828-000, Brazil
[c] Department of Environmental Sciences, Federal University of São Paulo, Diadema, Rua São Nicolau, 210, São Paulo, SP, 09913-030, Brazil
[d] Geological Survey of Israel, 32 Yeshayahu Leibowitz St, Jerusalem, 9691200, Israel

ARTICLE INFO

Keywords:
Fluvial sediments
Optically stimulated luminescence
Dosimetry
Geochronology

ABSTRACT

This study reports on the first investigation into the potential of quartz luminescence dating to establish formation ages of ferruginous duricrust deposits (ironstones) of the Xingu River in Eastern Amazonia, Brazil. The studied ironstones comprise sand and gravel cemented by goethite (FeO(OH)), occurring as sandstones and conglomerates in the riverbed of the Xingu River, a major tributary of the Amazon River. The Xingu ironstones have a cavernous morphology and give origin to particular habitat for benthic biota in an area that hosts the largest rapids in Amazonia. So far, the Xingu ironstones have uncertain formation ages and their sedimentary origin is still poorly understood. In this way, seven samples of ironstones distributed along the lower Xingu River were collected for optically stimulated luminescence (OSL) dating of their detrital quartz sand grains. Additionally, the organic content of some samples was dated by radiocarbon (^{14}C) for comparison with quartz OSL ages. The luminescence ages of the sand-sized quartz grains extracted from the ironstones were obtained from medium (100–300 grains) and small (10–20 grains) aliquots using the single aliquot regenerative-dose (SAR) protocol. Equivalent doses (D_e) distributions have varied overdispersion (OD) both for medium size aliquots (OD = 19–58 %) and small size aliquots (OD = 29–76 %). No significant trend was observed between D_e and aliquot size. The studied ironstones grow over the riverbed, but stay below or above water throughout the year due to the seasonal water level variation of the Xingu River. However, the effect of water saturation in dose rates is reduced due to relatively low porosity of ironstones. Water saturated dose rates (dry sample dose rates) range from 2.70 ± 0.21 (2.79 ± 0.22) Gy/ka to 12.34 ± 0.97 (13.26 ± 1.12) Gy/ka, which are relatively high when compared to values reported for Brazilian sandy sediments elsewhere (~1 Gy/ka). Samples with high overdispersion (>40 %) are mainly attributed to mixing of grains trapped in different time periods by goethite cementation. The obtained OSL ages for water saturated (dry) samples range from 3.4 ± 0.3 (3.3 ± 0.4) ka to 59.6 ± 6.0 (58.1 ± 6.4) ka, using D_e determined from medium size aliquots and dose response curves fitted by an exponential plus linear function. Radiocarbon ages of the bulk organic matter extracted from selected ironstone varied from ca. 4 cal ka BP to ca. 23 cal ka BP. Significant differences were observed between OSL and radiocarbon ages, suggesting asynchronous trapping of organic matter and detrital quartz within the ironstone matrix. These late Pleistocene to Holocene ages indicate that ironstones of the Xingu River result from an active surface geochemical system able to precipitate goethite and cement detrital sediments under transport. The obtained ages and differences between OSL and radiocarbon ages point out that the ironstones have multiphase and spatially heterogeneous growth across the Xingu riverbed. Our results also expand the application of luminescence dating to different sedimentary deposits.

* Corresponding author.
E-mail address: pontienn@usp.br (P. Niyonzima).

https://doi.org/10.1016/j.quageo.2021.101241
Received 17 November 2020; Received in revised form 5 October 2021; Accepted 9 October 2021
Available online 13 October 2021
1871-1014/© 2021 Elsevier B.V. All rights reserved.

1. Introduction

Weathering products with authigenic iron (Fe) minerals are widespread in soils and sediments of the tropical regions. However, their occurrence is peculiar in Eastern Amazonia, where fluvial sands and gravels are cemented by goethite (FeO(OH)) to form rocks (ironstones) that occur as patches over Precambrian bedrocks of the Xingu River (Sawakuchi et al., 2015). The ages of the Xingu ironstones are unknown and their formation process is still poorly understood despite their relevance as substrate for the aquatic ecosystems (Fitzgerald et al., 2018). Also, over the past decades, a growing number of studies have demonstrated the potential use of weathering clays, oxides and hydroxides as indicators of climatic changes in continental environments through mineral or isotopes markers (Giral-Kacmarcik et al., 1998; Girard et al., 2000, 2002). It has been reported that the original oxygen isotopic ratio of iron minerals such as goethite and hematite is generally preserved, thereby providing information about weathering and climate conditions prevailing at the time of ironstone formation (Giral-Kacmarcik et al., 1998; Girard et al., 2002). Additionally, absolute dating of ironstones remains an important and challenging task for constraining the evolution of the continental surfaces as well as to support their use for paleoclimate or relief reconstructions. Different dating methods of ironstones were applied in Brazilian settings, including (U-Th)/He of goethite (Riffel et al., 2016), electron paramagnetic resonance of matrix kaolinite (Allard et al., 2018) and cosmogenic nuclides of trapped quartz grains (^{10}Be) (Pupim et al., 2015). However, these methods are suitable to obtain ages in the hundred thousand to million years timescale and dating of ironstones is still difficult for the thousand years timescale necessary to cover the late Pleistocene and Holocene age range.

The main objectives of this work are to check the feasibility of optically stimulated luminescence (OSL) dating method on detrital quartz grains within ironstones and to shed light on the timing and processes of ironstones formation over the riverbed of the Xingu River. We focus on ironstones corresponding to sandstones and conglomerates cemented by goethite and with minor amount of organic matter and clay. We investigated the applicability of OSL dating using the single aliquot regenerative dose (SAR) protocol (Murray and Wintle, 2000, 2003) in quartz sand grains extracted from the ironstones framework. Additionally, the bulk organic matter from selected ironstone samples was dated by radiocarbon (^{14}C) for independent age control. The optimal luminescence measurements conditions for obtaining equivalent dose values of the samples were then examined, with quartz OSL ages being compared to radiocarbon ages from bulk organic matter. The geochronological dataset obtained in this study is crucial to the discussion about the origin of the Xingu ironstones.

2. Study area

The Xingu River is the fifth largest tributary of the Amazon River, with a drainage area of 504,300 km^2 (Filizola, 1999) in Eastern Amazonia (Fig. 1a and b). It is a clearwater river with a bedload dominated by fine to coarse sand, low concentration of suspended sediments (<100 mg/l) and water pH 5 to 6 (Sioli, 1984). The rainfall is controlled by the strength of the South American Monsoon System and by shifts of the Intertropical Convergence Zone (Marengo, 2004), which promote a

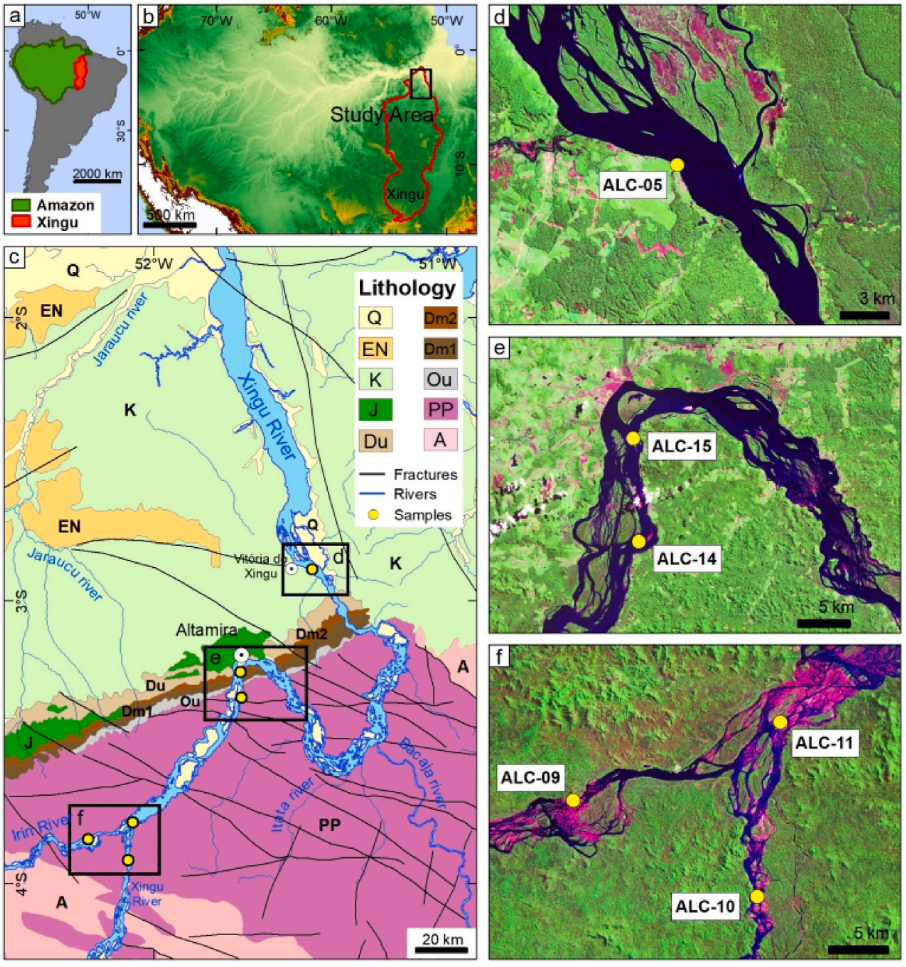

Fig. 1. Location of the Xingu River basin in Eastern Amazonia (a and b). Simplified geological map (c) and location of sampling sites (yellow dots in black rectangles and in d, e and f panels) in the lower Iriri and Xingu Rivers. Lithological units of the geological map (c): (A) Archean gneisses, granodiorites and granitoids (Xingu Complex) and metavolcanic and metasedimentary rocks; (PP) Paleoproterozoic granites, granodiorites and charnockites; (Ou) Ordovician–Devonian organic-rich shales and sandstones (Trombetas Group); (Dm1–Dm2–Du) Middle–Late Devonian shales, siltstones and sandstones (Urupadi and Curuá Groups); (J) Early Triassic diabase sills (Penatecaua magmatism); (K) Cretaceous sandstones and conglomerates (Alter do Chão Formation); (EN) Eocene–Neogene undifferentiated sediments and lateritic soil crusts; (Q) Quaternary undifferentiated sediments. Lithological mapping units according to Bahia et al. (2004). Background images in d, e and f are from Landsat GeoCover 1990) (https://earthexplorer.usgs.gov/). (For interpretation of the references to colour in this figure legend, the reader is referred to the Web version of this article.)

marked seasonality in the river water discharge. The mean annual water discharge is 9700 m^3/s (Filizola, 1999), but it ranges from 1000 m^3/s (September–October) during the dry season to 19,000 m^3/s (March–April) in the wet season (Bertassoli et al., 2019). The Xingu River shows high diversity in channel morphology, with a meandering channel at its upper catchment, a bedrock channel with multiple flow paths in the middle course, and a fluvial ria in its downstream section (Sawakuchi et al., 2015; Bertassoli Jr et al., 2019).

After the confluence with the Iriri River, the Xingu flows to northeast over Precambrian metamorphic and igneous rocks of the Brazilian shield until reaching the border of the Paleozoic-Mesozoic Amazonas sedimentary basin, where it bends to southeast and to northeast again to follow the way until the Amazon River (Fig. 1c). This sector of the Xingu River is called "Volta Grande do Xingu", which has great relevance for Amazonian ecosystems due its high biodiversity and a high degree of endemism of the ichthyofauna (Nogueira et al., 2010). In the Volta Grande, the Xingu is a bedrock anastomosing system characterized by a 4–5 km width valley segmented into multiple interconnected crisscross channels with rapids bounding sediment bars covered by riparian vegetation and rainforest (Sawakuchi et al., 2015).

The morphology of the Xingu River turns to a straight, narrow and deep channel from the point that it flows over sedimentary rocks of the Amazonas basin. This zone represents a knick point that separates the bedrock-dominated channel from the fluvial ria in its lower course (Fig. 1c). The Xingu Ria can reach up to 14 km wide and 180 km long, with estuarine-like hydrodynamics due the strong influence of the backwater effect of the Amazon River, waves and tides (Meade et al., 1991). The studied ironstones samples were collected in sites of the Iriri and Xingu Rivers, mainly in sectors draining the Precambrian metamorphic and igneous rocks, but also in sectors over Paleozoic-Mesozoic sedimentary rocks (Fig. 1c–f).

3. Methods

3.1. Samples collection and description

Seven samples representative of ironstones occurring in the lower Iriri and Xingu Rivers were collected using hammer and chisel during the dry season for luminescence dating. The location of each sample is shown in Fig. 1. Three samples were also selected for radiocarbon dating of bulk organic matter. The samples were retrieved from sites lying over granitoids and sedimentary rocks that constitute the riverbed of the Iriri and Xingu Rivers in the study area (Fig. 2). The Xingu ironstones have a cavernous morphology and are mainly composed of goethite matrix with detrital quartz sand grains, granules and pebbles (Fig. 3).

The textural and mineralogical characterization of sandy ironstones was performed using light polarized microscopy (LPM). All analyses were carried out at the Institute of Geosciences of the University of São Paulo (USP). Thin sections (30 μm thickness) were used for LPM analyses using a Carl Zeiss Axioplan 2 microscope, with LAS-Leica Application Suite software for imaging.

3.2. Luminescence dating

3.2.1. Sample preparation

The preparation of detrital quartz concentrates for luminescence dating was performed under subdued orange/red light using conventional laboratory procedures (Mejdahl and Christiansen, 1994). The outer surface of each sample was removed to avoid material possibly exposed to light. This portion was kept for gamma ray spectrometry to determine radionuclides concentrations needed for dose rate calculation. The inner parts of the samples were protected from light to ensure that the sediments retain their natural luminescence signal. This portion was carefully crushed and disaggregated to release the sand grains.

Detrital grains in the size range of 180–250 μm were recovered by wet-sieving. The target fraction was treated with hydrogen peroxide (H_2O_2, 27 %) to remove organic matter and hydrochloric acid (HCl, 10 %) to remove carbonate minerals. Heavy minerals and feldspar grains were removed by heavy liquid separation with lithium metatungstate solutions at densities of 2.75 g/cm^3 and 2.62 g/cm^3, respectively. To further purify and concentrate the quartz fraction and to remove the outer α–irradiated layer of quartz grains, the samples were etched in 38 % HF for 40 min. Infrared (IR) stimulation was performed to confirm the absence of feldspar contamination in the HF-treated quartz fraction. Samples with remaining feldspar were subjected to repeated cycles of etching with 5 % HF for 24 h followed by wet sieving (180 μm) until a

Fig. 2. Field view of ironstones in the riverbed of the Xingu River exposed during the dry season. a) Rocky riverbed (migmatites and gneisses). b) Meter-scale patches of ironstones over the Xingu riverbed. c,d) Thick goethite crust with cavernous morphology.

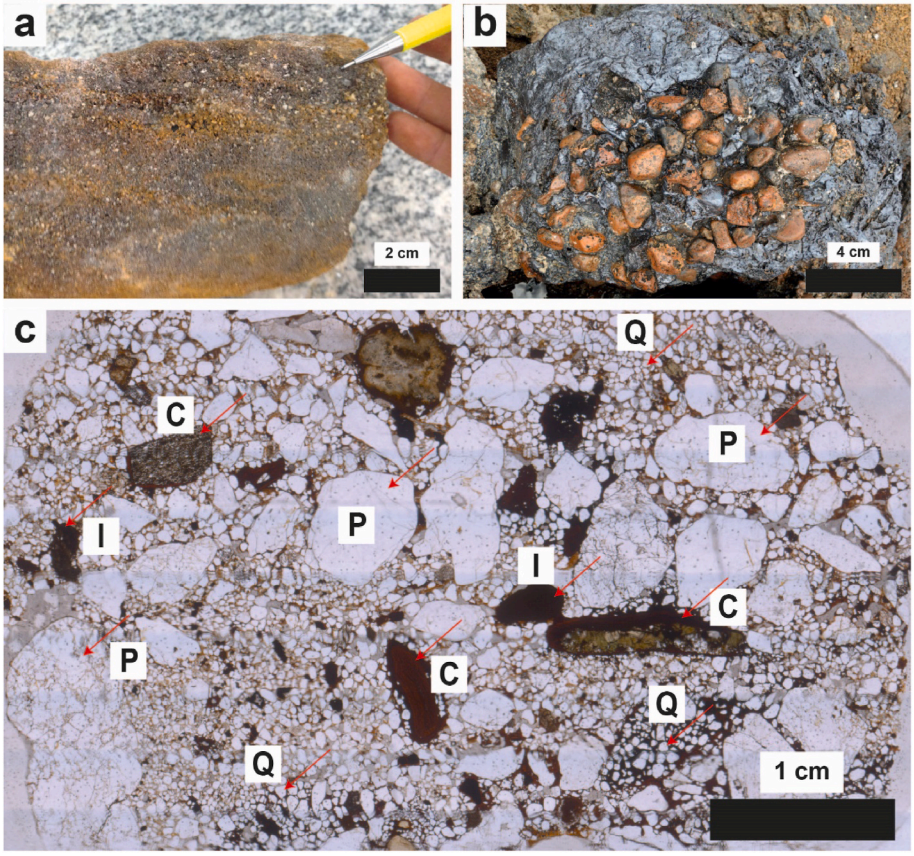

Fig. 3. Macroscopic and microscopic views of the Xingu ironstones. a) Sandstone with goethite cement (site ALC-05). b) Conglomerate of well-rounded quartz pebbles cemented by goethite. c) Thin section view of conglomeratic sandstone (site ALC-15) with framework composed of monocrystalline quartz (Q), polycrystalline quartz (P), goethite coated grains (C) and iron oxide intraclasts (I), and cemented by goethite. Red arrows point grain types named by the respective label. (For interpretation of the references to colour in this figure legend, the reader is referred to the Web version of this article.)

negligible IR signal (compared with blue stimulation signal) was achieved.

3.2.2. Equivalent dose measurement procedures

All luminescence measurements were carried out on an automated Risø TL/OSL DA-20 reader at the Luminescence and Gamma Spectrometry Laboratory (LEGaL) of the Institute of Geosciences, University of São Paulo. The reader is equipped with $^{90}Sr/^{90}Y$ beta source that delivers a dose rate of 0.119 ± 0.001 Gy/s, infrared (870 ± 20 nm; 145 mW/cm^2) and blue light-emitting diodes (470 ± 20 nm; 80 mW/cm^2) operating at 90 % of their powers for stimulation and 7.5 mm Hoya U-340 filter for light detection in the ultraviolet band (290–340 nm) with a bialkali PM tube (Thorn EMI 9635QB) (Bøtter-Jensen et al., 2000). The SAR protocol proposed by Murray and Wintle (2000, 2003), as described in Table 1, was used to obtain equivalent doses (D_e) for all samples. The SAR sequence consisted of four regeneration doses, a recuperation (zero dose) point and a recycling point. The regeneration doses were chosen to bracket the expected D_e, allowing it to be evaluated by interpolation. For all aliquots used in luminescence measurements, the purity of the quartz was checked by an IR depletion ratio (Duller, 2003). Only aliquots with recycling ratio between 0.90 and 1.10, recuperation less than 5 % (of the natural signal) and IR depletion ratio within 10 % of unit were considered for D_e estimation. The corrected OSL signal (L_x/T_x) was calculated using the initial 0.8 s of OSL decay curve minus the background estimated from the last 10 s of light emission. Preheat plateau and dose recovery tests were carried out to set up the best preheat temperatures to estimate equivalent doses.

For each sample, 24 to 36 medium quartz aliquots (100–300 grains) were prepared for measurements. For better interpretation of D_e distributions, two samples with high overdispersion (OD > 40 %) and one sample with moderated OD (29 %) were also measured using small aliquots (10–20 grains). Dose response curves (DRC) were fitted to the data with a single saturating exponential equation. However, the dosimetric behavior of OSL signals was also investigated by fitting DRCs using exponential plus linear function. For both cases, the D_e was estimated by interpolating the sensitivity-corrected natural OSL signal onto the dose response curve.

The aliquots with D_e greater than two times the value of characteristic dose ($2D_0$) of DRCs described by a single exponential function were also rejected for the analysis (Wintle and Murray, 2006). As fluvial sediments from different settings of Brazil are relatively well bleached (Sawakuchi et al., 2016; Pupim et al., 2016), the central age model (CAM) (Galbraith et al., 1999) was considered appropriate for equivalent dose estimation. Data analysis was carried out using Analyst (Duller, 2015), Origin and Luminescence R package (Kreutzer et al., 2012) softwares.

Table 1
The SAR protocol applied for this study (Murray and Wintle, 2003). Four regeneration doses (D_1 to D_4) were used to build the dose response curve. A constant test dose (D_t) was used to calculate the corrected OSL signals (L_x/T_x). Recuperation was calculated through the ratio between D_5 (0 Gy) and natural dose (D_n) signals. Signals from D_6 and D_1 were used to calculate recycling ratios. IR stimulation was performed before the measurement of D_7 signal to appraise feldspar contamination.

Step	Treatment
1	Give dose, D_x (D_n = natural signal; $D_1<D_2<D_3<D_4$; D_5 = 0 Gy; $D_6 = D_7 = D_1$)
2	Preheat at 260 °C for 10 s
3	Blue light stimulation for 40 s at 125 °C (L_x)
4	Give test dose, D_t
5	Cut-heat at 160 °C for 0 s
6	Blue light stimulation at 125 °C for 40 s (T_x)
7	Blue light illumination at 280 °C for 40 s
8	Return to step 1

Table 2
Geographical coordinates and altitude of the sampling sites and densities and maximum water saturation of studied samples.

Field code	Lab code	Longitude	Latitude	Altitude (m)	Density (g/cm^3)	Maximum water saturation (%)
ALC-11-1	L1244	−3°46'56.81"	−52°34'19.21"	117	2.62	3.2
ALC-09-2	L1245	−3°50'32.10"	−52°43'50.17"	126	2.41	6.4
ALC-15-1	L1246	−3°15'03.52"	−52°11'37.28"	86	2.35	3.4
ALC-05-04	L1247	−2°53'19.12"	−51°56'25.36"	2	2.50	3.4
ALC-10-1A	L1264	−3°55'00.21"	−52°35'23.67"	126	2.24	3.0
ALC-15-1A	L1265	−3°15'03.52"	−52°11'37.28"	86	2.87	3.0
ALC-14	L1266	−3°20'29.03"	−52°11'20.24"	92	2.87	1.5

3.2.3. Determination of radionuclides concentrations and dose rate calculation

The concentrations of uranium (^{238}U), thorium (^{232}Th) and potassium (^{40}K) were determined using high-resolution gamma spectrometry through a high-purity germanium (HPGe) detector with a 55 % relative efficiency and 2.1 keV energy resolution, encased in an ultralow background shield (Canberra industries). The outer surface of each sample was milled and 278–445 g of dry samples were packed in plastic containers and sealed. Gamma ray spectrometry was performed after sample storage for at least 28 days for radon to reach equilibrium with its parent radionuclides. The beta and gamma dose rates were calculated using the concentrations of ^{238}U, ^{232}Th and ^{40}K and conversion factors from Guérin et al. (2011). The cosmic-ray dose rates were calculated according to Prescott and Hutton (1994), taking into consideration the altitude and geomagnetic latitude of the sampling site and density (Table 2) of the overlying ironstones. Average depth of 0.10 ± 0.05 m was used to calculate the cosmic dose rate for all samples, since they were retrieved from surface ironstones layers. The samples were dry rocks when collected, but they experience an underwater period during the wet season. Hence, the dose rates were calculated taking minimum (dry sample) and maximum water saturation (water weight and dry sample weight). Maximum water saturation values (Table 2) were obtained by keeping samples underwater in the laboratory.

3.3. Radiocarbon dating

Four samples had a significant amount of organic matter, as indicated by reaction to hydrogen peroxide (H_2O_2, 27 %), and therefore were selected for radiocarbon dating. Fresh subsamples from the core of the selected specimens were pulverized, pretreated with HCl to ensure the absence of carbonates, and dated by Accelerator Mass Spectrometry (AMS) at Beta Analytic Laboratory, Miami, Florida, USA. Radiocarbon (^{14}C) ages of the bulk organic fraction were calibrated using Calib 7.1 (Stuiver et al., 2019) and the SHCal20 database (Hogg et al., 2020). Stable carbon isotopic signatures (δ^{13}C) of the organic fraction were measured at the same laboratory using an Isotope Ratio Mass Spectrometer (IRMS).

4. Results

4.1. Ironstones characteristics

All studied ironstone types (sandstones, conglomeratic sandstones and conglomerates) form tabular beds irregularly covering the riverbed of the Iriri and Xingu Rivers. The sandstones have a framework (80–85 % of the rock) mainly composed of quartz sand grains cemented by goethite (15–20 %). The sand grains consist of monocrystalline quartz (15–35 %), polycrystalline quartz (20–30 %), lithic fragments of schist (5–10 %), ferruginous-coated grains (15–20 %) and iron oxide grains interpreted as intraclasts of ironstones matrix (1–2 %) (Fig. 3a,c). Conglomerates have a framework of rounded quartz pebbles and a sandy matrix cemented by goethite (Fig. 3b).

4.2. OSL and radiocarbon ages

Quartz from the ironstones of the Xingu River has high luminescence sensitivity, with OSL decay curve dominated by the fast component. The dose response curves follow a single saturating exponential function, with average $2D_0$ value up to 284.4 ± 83.4 Gy (sample L1247). Fig. 4 shows examples of natural OSL decay curves and dose response curves of different aliquots from samples L1244 and L1247.

A preheat temperature test was carried out to ensure the selection of the most suitable thermal treatment to run the SAR protocol for D_e estimation. Three samples (L1244, L1245 and L1247) were used for this experiment. Three aliquots for each sample were initially bleached for 100 s at 25 °C using blue LEDs at 90 % power to remove the natural signal. The bleached aliquots were then irradiated with a beta dose of 50 Gy and sensitivity-corrected OSL signals were measured at various preheat temperatures ranging from 180 °C to 300 °C (20 °C intervals) with cut-heat at 160 °C. The sensitivity-corrected OSL signal for the given dose of 50 Gy was plotted in function of different preheat temperatures (Fig. 5), indicating that corrected OSL signals for our samples did not change significantly for preheat temperatures ranging from 200 °C to 260 °C.

We performed dose recovery tests on quartz aliquots of samples L1244, L1245 and L1266 using given beta doses of 15, 50, 100 and 200 Gy. This dose range was selected from a preliminary set of D_e measurements made on each of the studied samples. Aliquots were firstly bleached using a blue LED stimulation at room temperature (~25 °C) for 300 s before irradiation. Afterwards, dose recovery tests for a given dose of 50 Gy were carried out on aliquots of samples L1245 and L1245 using the protocol described in Table 2, with the preheat temperatures between 180 °C and 280 °C. Calculated-to-given ratios were between 0.83 ± 0.02 and 1.05 ± 0.07 (Fig. 6).

The preheat temperature of 260 °C represents the best performance on dose recovery tests performed for a given dose of 50 Gy, considering not only the calculated-to-given dose ratios of 0.92 ± 0.02 (L1245) and 1.05 ± 0.07 (L1266), but also the recycling ratios closer to unity and lower recuperation values. Thus, additional dose recovery tests were carried out on sample L1244 using given doses of 15, 50, 100 and 200 Gy and preheat temperature of 260 °C (Fig. 7). For this purpose, sixteen aliquots of sample L1244 were firstly bleached using a solar simulator for 24 h and four aliquots were used for each given dose. In this test, doses were estimated through fitting the DRCs by both saturating single exponential and exponential plus linear functions. Similar equivalent doses were obtained from DRCs described by single saturating exponential and exponential plus linear functions (Fig. 7). The calculated-to-given dose ratios obtained using a single saturating exponential DRC were 0.98 ± 0.07, 0.91 ± 0.05, 0.89 ± 0.08 and 0.85 ± 0.18 for given doses of 15, 50, 100 and 200 Gy, respectively. We observed increasing D_e underestimation for given doses of 100 and 200 Gy using both fitting functions. For doses up to 50 Gy, calculated-to-given dose ratios are within 10 % of unity. These dose recovery experiments supported the choice of 260 °C preheat temperature to estimate D_e in the studied ironstone samples.

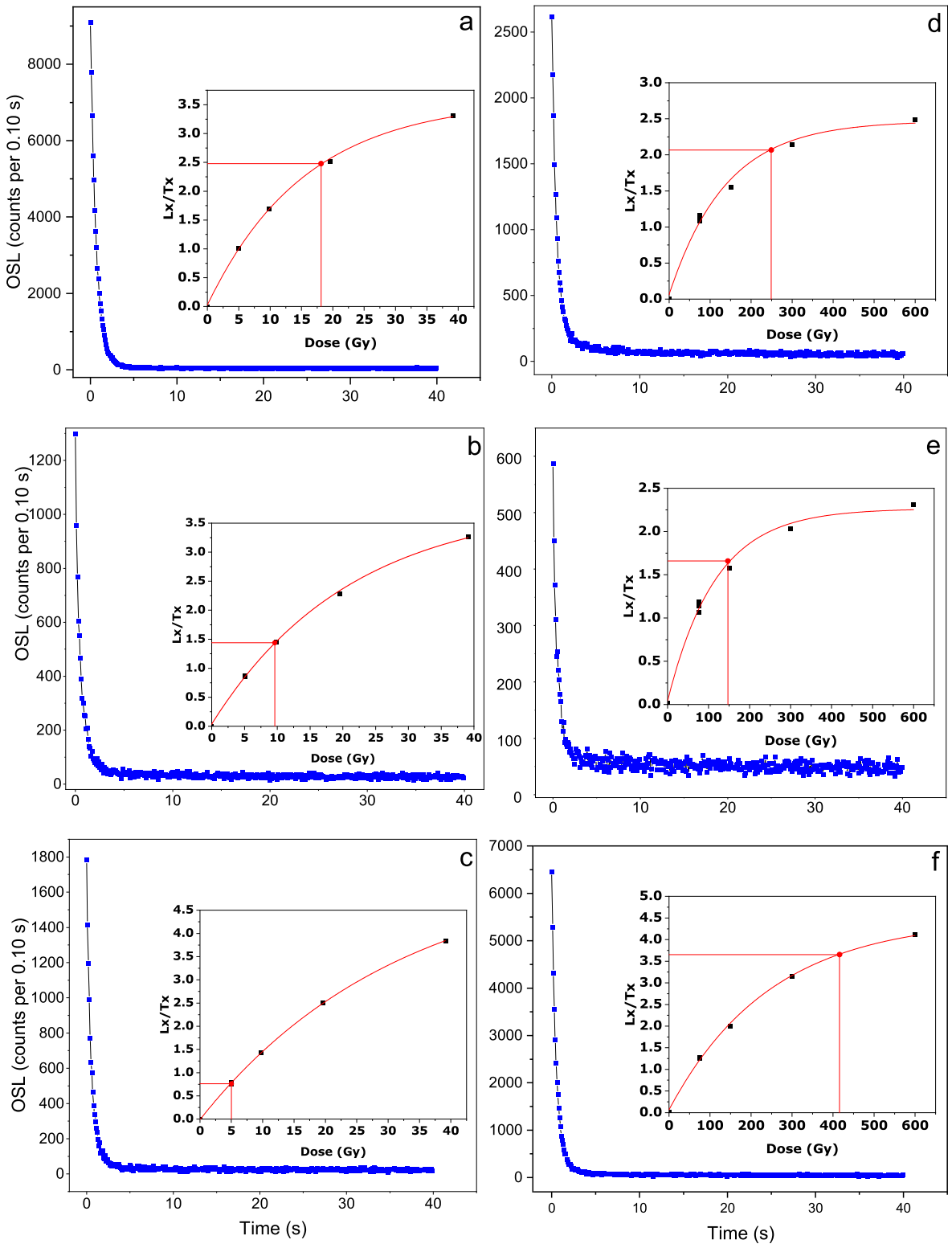

Fig. 4. Representative natural OSL decay curves and corresponding sensitivity-corrected dose response curves (insets) for aliquots of samples L1244 (a, b and c) and L1247 (d, e and f). Interpolated values in dose response curves correspond to natural signals and equivalent doses.

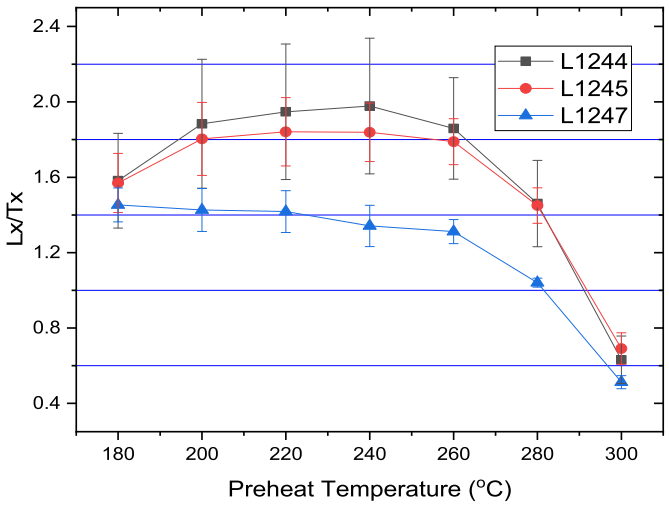

Fig. 5. Sensitivity-corrected OSL signal (L_x/T_x) from a given dose of 50 Gy against the preheat temperature between 180 °C and 300 °C. Each data point represents the average of three aliquots with its respective standard deviation as error bars.

4.3. Dose rates, equivalent doses and ages

The ironstone samples have densities from 2.41 to 2.87 g/cm^3 and maximum water saturation up to 6.4 % (Table 2). Cosmic dose rates are relatively uniform, with values of 0.23 and 0.24 Gy/ka (Table 3). The Xingu ironstones have large variation in radionuclides concentrations, with ^{238}U and ^{232}Th concentrations respectively reaching up to 19 and 122 ppm (Table 3). The high ^{238}U and ^{232}Th concentrations give relatively high dose rates up to ~13 Gy/ka (Table 4). Since the exact time that the samples spend under water is unknown, a range of total dose rates were calculated assuming water saturated samples and dry samples. Thus, water saturated and dry dose rates (Table 3) of each sample were used in the age calculation.

The D_e values determined using the CAM for medium aliquots are relatively higher than values from small aliquots, but there is no clear relationship between aliquot size and overdispersion (OD) of equivalent dose distributions (Table 4). Abanico plots for both medium and small size aliquots for samples L1246, L1247 and L1266 are presented on Fig. 8. Abanico plots for other samples (L1244, L1245, L1264 and L1265) are also presented on Fig. 9. The medium size aliquots gave D_e values ranging from 13.6 ± 0.9 Gy to 230.5 ± 13.1 Gy when the DRCs are fitted by single saturating exponential function, with OD values ranging from 19 % to 58 %. However, in the dose range beyond 100 Gy, DRCs are better fitted by exponential plus linear function, which gave D_e values higher than the values, obtained using the single saturating exponential function (Table 5). Ages calculated from water saturated dose rates and exponential plus linear function D_e vary between 3.4 ± 0.3 and 59.9 ± 6.0 ka. Ages calculated using dry or water saturated dose rates overlap by their errors. Table 5 presents a summary of D_e, dose rates and calculated ages.

Calibrated radiocarbon ages of organic matter extracted from samples L1244, L1264, L1245 and L1265 range between ca. 4.5 and 23 cal ka BP. OSL ages were older or younger than radiocarbon ages obtained in the corresponding samples. Calibrated ages and conventional radiocarbon ages, δ^{13}C values of organic matter and OSL ages are presented in Table 6.

5. Discussion

5.1. OSL ages uncertainties

5.1.1. Sources of overdispersion in the equivalent dose distributions

The D_e distributions for medium and small size aliquots of the analyzed samples clearly show a varied scatter, with OD values between 19 and 76 %. For D_e distributions obtained using medium size aliquots, sample L1265 has low OD of 19 %, pointing to a single population of grains with doses centered on the weighted mean D_e value. Another sample (L1266) has D_e distributions with high OD up to 67 %. However, most of our samples have D_e with OD values in the range of 29–35 %, consistent with the commonly reported range for heterogeneous, but relatively well-bleached sediments, i.e, majority of grains was fully bleached and not affected by post-depositional mixing (Arnold et al., 2007; Arnold and Roberts, 2009).

For medium aliquots (100–300 grains), at least part of resulting OSL signals will be affected by averaging effects (Arnold and Roberts, 2009). Thus, measurements using small aliquots were performed in order to minimize averaging effects, highlighting D_e variations among grains of the same sample. In the studied samples, small aliquots (10–20 grains) show D_e distributions with lower or higher OD (up to 76 %), but presenting systematically lower D_e values when compared to medium aliquots (Table 4). This suggests that the contribution of grains with higher D_e increases from small to medium aliquots. The variation in D_e due to aliquot size as well as the high OD of some samples point out to significant D_e variability among quartz grains hosted in ironstones.

The most likely interpretation of high OD in D_e distributions from

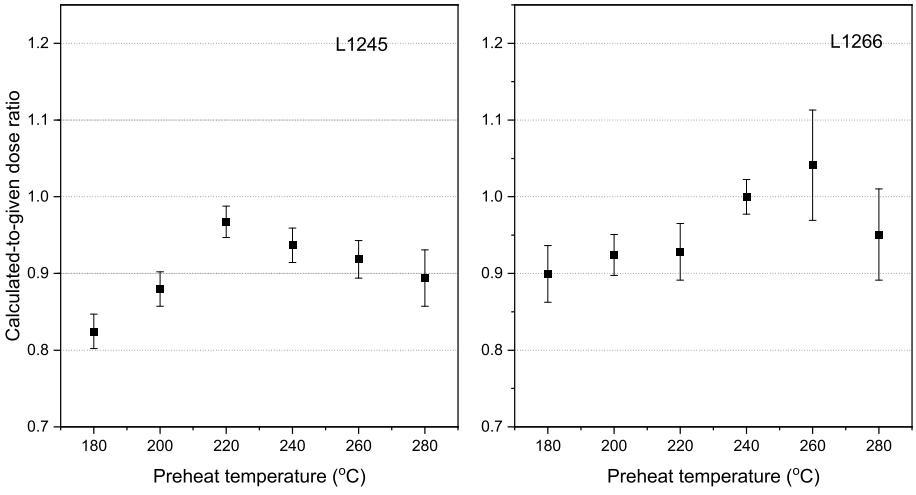

Fig. 6. Calculated-to-given dose ratios obtained through dose recovery tests using samples L1245 and L1266. Three aliquots were measured for each data point using a given dose of 50 Gy. The equivalent doses were calculated using the Central Age Model (CAM) and 1 σ was used as error bar.

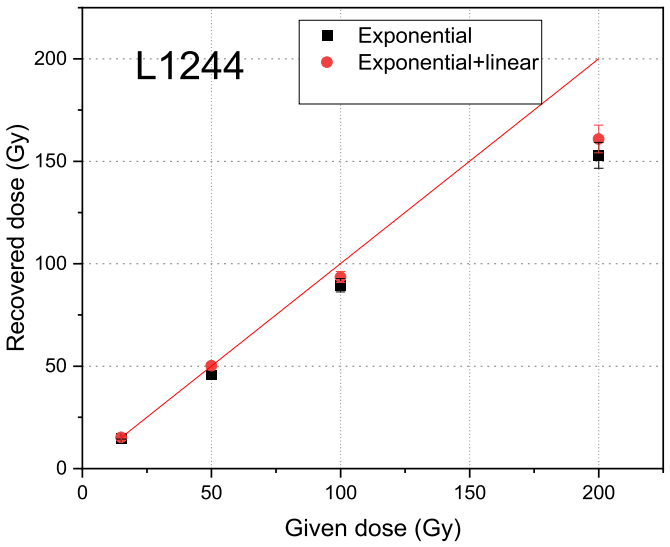

Fig. 7. Given dose against recovered dose for quartz aliquots from sample L1244. Four aliquots were measured for each given dose (15, 50, 100 and 200 Gy). The recovered doses were calculated using the Central Age Model (CAM) with its standard error at 1 σ as error bar. The unity line was added for easy evaluation of given and recovered doses.

fluvial sediments is that grains were incompletely and heterogeneously bleached prior to deposition (Wallinga, 2002; Rodnight et al., 2005). This interpretation is not supported for the studied river by the fact that quartz grains from fluvial sediments of the Xingu River (Pupim et al., 2016) and of other cratonic rivers in Brazil are well bleached (Sawakuchi et al., 2016). Post-depositional sediment mixing due to the movement of grains by natural processes such as bioturbation and pedogenesis is another potential source of variability in D_e distributions (David et al., 2007; Jacobs and Roberts, 2007). However, the high degree of cementation of the studied samples makes post-depositional grain mixing negligible. The scatter in D_e distributions can also be attributed to intrinsic differences in the luminescence sensitivity of different measured aliquots (Tsakalos et al., 2018), but this effect should be minimal in the studied samples due to the high sensitivity of their quartz grains. Heterogeneities in density of sedimentary matrix (Nathan et al., 2003) and small-scale variations in the beta radiation dose rate to which the samples have been exposed during burial (Jacobs and Roberts, 2007) are also potential factors contributing to overdispersion in D_e distributions from quartz sand grains. Dose rate heterogeneities would be more important in conglomeratic ironstones, where quartz pebbles can promote zones of low dose rate compared to the goethite matrix, which concentrates ^{238}U and ^{232}Th. Thus, quartz sand grains laying nearby quartz pebbles would be submitted to lower dose rate field compared to quartz grains immersed in the goethite matrix. The break up of granules or pebbles during sample preparation could also contribute for D_e variation within sample. In this case, fragments derived from the inner portion of granules or pebbles should have saturated OSL signals, contributing to a high dose tail of the D_e distributions. However, this possibility is reduced as saturated aliquots were not observed in the younger samples.

The studied ironstones would be formed by successive phases of goethite precipitation and trapping of quartz grains through a timespan. This could explain the significant variation of D_e from aliquots of the same sample as well as the differences between ages of detrital organic matter and quartz grains. Thus, mixing of grains trapped during different time periods could be a major source of dispersion in D_e distributions from the studied ironstones. In this case, D_e determined using multigrain aliquots and CAM would represent the average population of grains trapped in the sampled ironstone layer. In the studied samples, the use of a relatively thin ironstone layer (~10 cm thickness) for extraction of quartz grains should minimize this effect. However, we recommend further studies using a single grain dating approach combined with petrographic methods to discriminate specific goethite cementation and grain trapping phases.

5.1.2. OSL signal saturation

The upper limit of the OSL dating on quartz is defined by signal saturation, and by assuming first order kinetics whereby a single electron trap/recombination center is involved in OSL signal used for dating. In this case, a single saturating exponential function would be expected to fit an OSL dose response curve and the recommended upper dose limit is defined by two times the characteristic dose ($2D_0$) (Wintle and Murray, 2006). The average $2D_0$ of the studied quartz is 284.4 ± 83.9 Gy, which is relatively high, but within the range of values reported in the literature (Mineli et al., 2021). Additional linear function is predicted for doses greater than 125 Gy (Wintle and Murray, 2006), however

Table 4
Equivalent doses (D_e) and overdispersion (OD) values calculated using the Central Age Model (CAM) for medium and small size aliquots from selected samples. Dose response curves were fitted by a single saturating exponential function. Field codes are presented in Table 2.

Lab code	Medium aliquots		Small aliquots	
	D_e (Gy)	OD (%)	D_e (Gy)	OD (%)
L1246	18.3 ± 2.3	58	13.0 ± 1.3	34
L1247	230.5 ± 13.1	29	201.3 ± 35.9	49
L1266	150.3 ± 13.2	49	73.3 ± 16.2	76

Table 3
Summary of radionuclides concentrations, dry and water saturated (WS) gamma and beta dose rates and cosmic dose rates (DR) for the studied samples. Field codes are in Table 2.

Lab code	^{238}U (ppm)	^{232}Th (ppm)	K (%)	$^{232}Th/^{238}U$	Dry gamma DR (Gy/ka)	WS gamma DR (Gy/ka)	Dry beta DR (Gy/ka)	WS beta DR (Gy/ka)	Cosmic DR (Gy/ka)
L1244	9.12 ± 0.41	19.98 ± 0.63	0.38 ± 0.02	2.2	2.07 ± 0.05	1.99 ± 0.23	1.93 ± 0.06	1.85 ± 0.23	0.23 ± 0.02
L1245	15.89 ± 0.55	122.17 ± 3.37	0.54 ± 0.02	7.7	7.76 ± 0.17	7.23 ± 0.78	5.27 ± 0.12	4.88 ± 0.58	0.23 ± 0.02
L1246	6.52 ± 0.23	29.35 ± 0.86	0.42 ± 0.01	4.5	2.24 ± 0.05	2.16 ± 0.24	1.84 ± 0.04	1.77 ± 0.22	0.23 ± 0.02
L1247	19.88 ± 0.68	0.29 ± 0.09	0.01 ± 0.01	0.01	2.24 ± 0.08	2.15 ± 0.25	2.57 ± 0.93	2.47 ± 0.31	0.23 ± 0.02
L1264	4.70 ± 0.18	12.13 ± 0.40	1.13 ± 0.05	2.6	1.39 ± 0.03	1.34 ± 0.15	1.76 ± 0.05	1.70 ± 0.21	0.24 ± 0.02
L1265	4.92 ± 0.18	16.85 ± 0.53	0.17 ± 0.01	3.4	1.40 ± 0.03	1.35 ± 0.15	1.15 ± 0.03	1.11 ± 0.14	0.23 ± 0.02
L1266	7.12 ± 0.25	55.35 ± 1.56	0.23 ± 0.01	7.8	3.50 ± 0.08	3.44 ± 0.39	2.37 ± 0.05	2.32 ± 0.29	0.23 ± 0.02

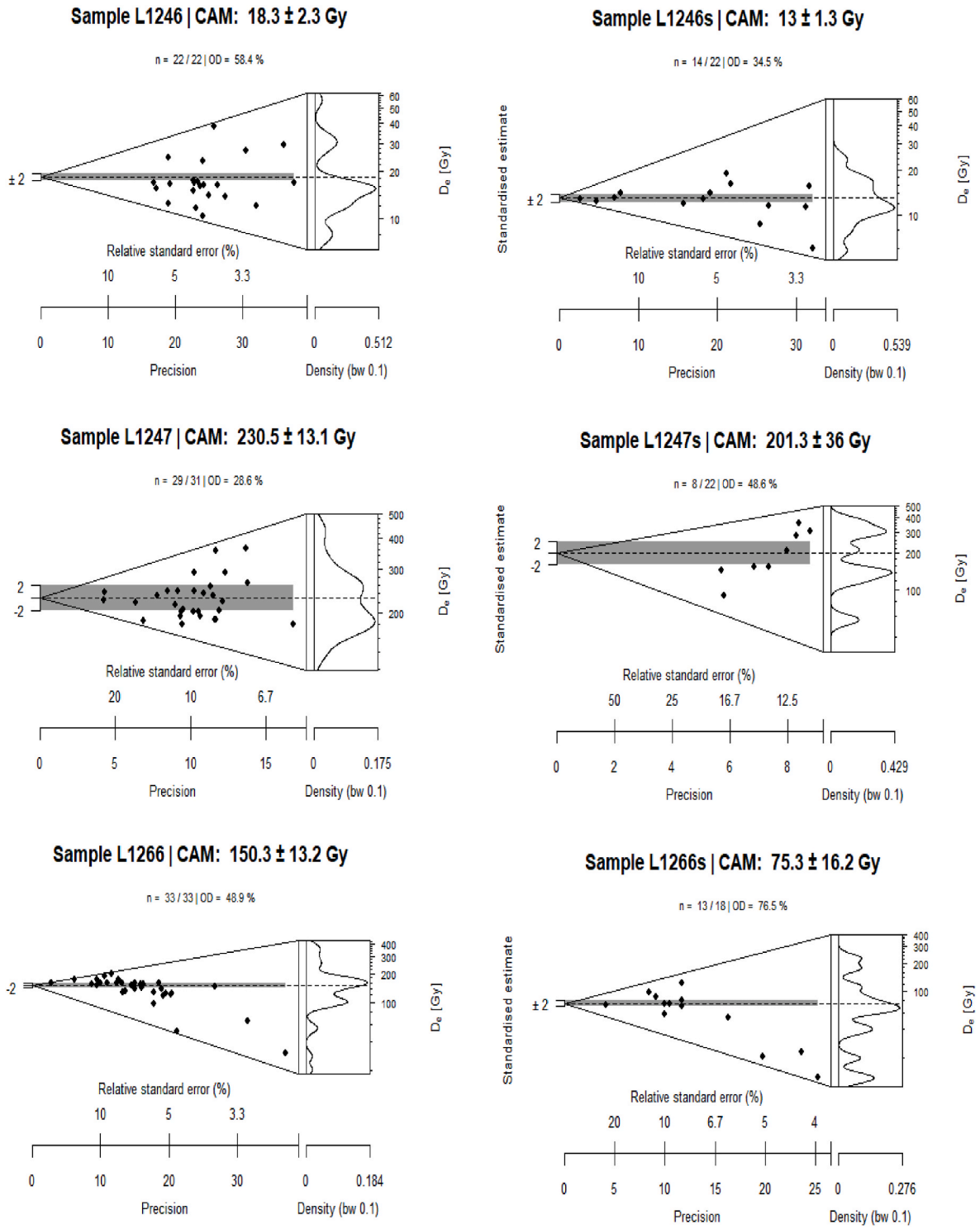

Fig. 8. Abanico plots of D_e values obtained using medium (left column) and small (right column) size aliquots for selected samples. The "s" in samples codes (L1246s, L1247s and L1266s) identifies equivalent dose distributions from small aliquots. The numbers of accepted and measured aliquots are indicated by "n". The samples equivalent dose (CAM) is indicated by the dashed line. The grey shaded band shows D_e range within its 2σ.

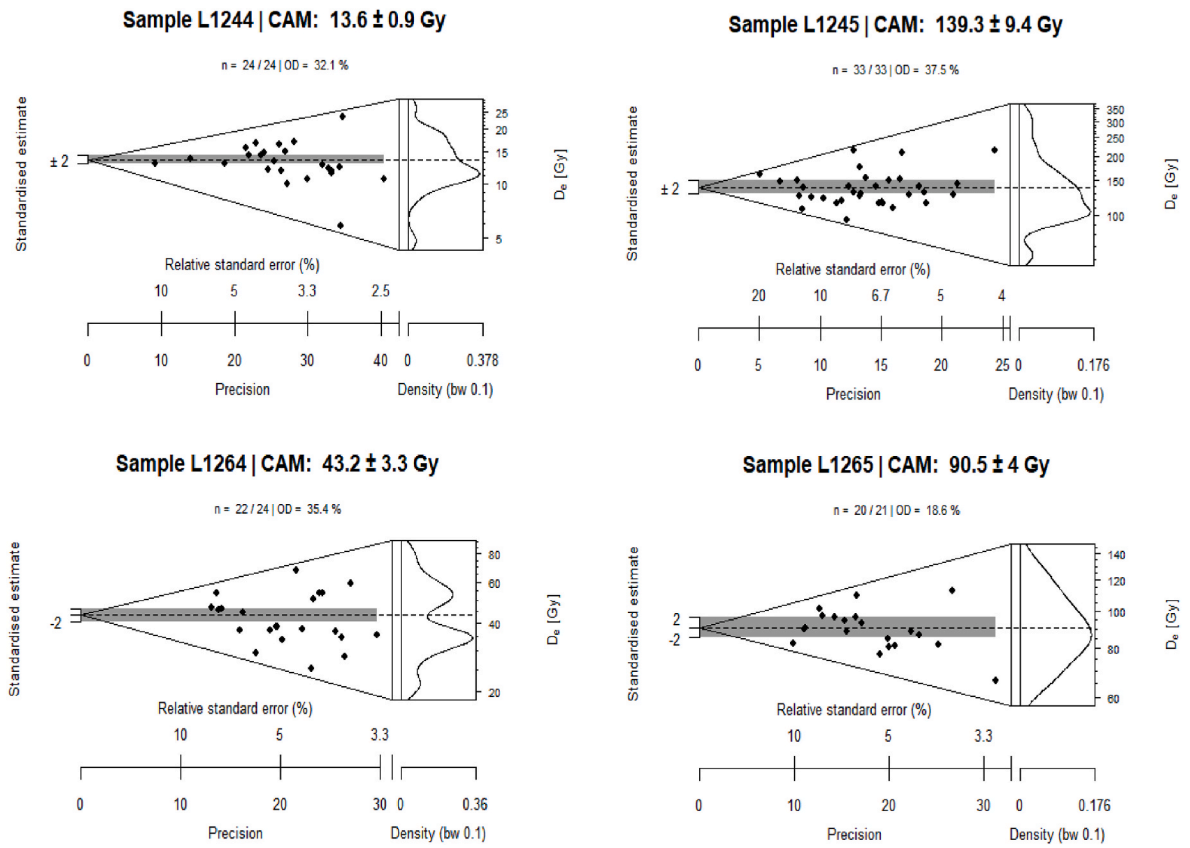

Fig. 9. Abanico plots showing D_e distributions from medium aliquots of samples L1244, L1245, L1264 and L1265. The numbers of accepted and measured aliquots are indicated by "n". The samples equivalent dose (CAM) is indicated by the dashed line. The grey shaded band shows D_e range within its 2σ.

Table 5
Equivalent doses (D_e) and ages calculated using the Central Age Model (CAM) for medium size aliquots by fitting the DRCs with both single saturating exponential (Exp) and exponential plus linear functions (Exp + lin). OSL ages were calculated using maximum water saturation (WS) and dry sample (DS) dose rates (DR). Field codes are presented in Table 2.

Lab code	Exp D_e (Gy)	Exp + lin D_e (Gy)	Total WS DR (Gy/ka)	Total DS DR (Gy/ka)	WS Exp OSL age (ka)	DS Exp OSL age (ka)	WS Exp + lin OSL age (ka)	DS Exp + lin OSL age (ka)
L1244	13.6 ± 0.9	14.0 ± 0.9	4.08 ± 0.32	4.22 ± 0.35	3.4 ± 0.3	3.2 ± 0.3	3.4 ± 0.4	3.3 ± 0.4
L1245	139.3 ± 9.4	163.8 ± 17.4	12.34 ± 0.97	13.26 ± 1.12	11.3 ± 1.2	10.5 ± 1.2	13.3 ± 1.8	12.4 ± 1.7
L1246	18.3 ± 2.3	18.4 ± 2.5	4.17 ± 0.33	4.31 ± 0.36	4.4 ± 0.7	4.3 ± 0.7	4.4 ± 0.4	4.3 ± 0.7
L1247	230.5 ± 13.1	290.8 ± 16.6	4.85 ± 0.40	5.03 ± 0.43	47.6 ± 4.8	45.8 ± 4.7	59.9 ± 6.0	58.1 ± 6.4
L1264	43.2 ± 3.3	46.3 ± 3.9	3.27 ± 0.26	3.38 ± 0.28	13.2 ± 1.5	12.8 ± 1.4	14.2 ± 1.6	13.9 ± 1.8
L1265	90.5 ± 4	88.8 ± 4.6	2.70 ± 0.21	2.79 ± 0.22	33.6 ± 3.0	32.5 ± 2.9	33.0 ± 3.1	32.3 ± 3.9
L1266	150.3 ± 13.2	164.5 ± 16.4	6.00 ± 0.50	6.09 ± 0.51	25.1 ± 3.1	24.7 ± 3.0	27.5 ± 3.5	27.1 ± 3.6

processes that influence the dosimetric characteristics of OSL are still unknown for this high dose linear component (Timar-Gabor et al., 2012). In our study, DRCs for samples with high D_e (>100 Gy) are best fitted by exponential plus linear function. Nevertheless, both single saturating exponential and exponential plus linear functions show dose underestimation as demonstrated by dose recovery tests (Fig. 7). Thus, age underestimation should be considered for samples L1245, L1247 and L1266, which presented D_e beyond 100 Gy (Table 5). In this way, the ages reported for these samples should be considered as minimal.

5.1.3. Dose rate considerations

The Xingu ironstones have relatively high radionuclides concentrations and most samples have dose rates higher than 4 Gy/ka, with a dry sample reaching a dose rate of 13 Gy/ka (Table 5). The overall dose rates are high compared to the doses rates commonly found in Brazilian sediments, which are mostly in the range of 0.4–3.1 Gy/ka (Pupim et al., 2016, 2019; Guedes et al., 2013; Sawakuchi et al. 2008, 2016; Soares et al., 2010; Ribeiro et al., 2015). Hence, the relatively high dose rate implies upper age limit of approximately ~71 ka for quartz OSL dating, considering maximum dose of around 284 Gy ($2D_0$) and dose rate of 4 Gy/ka. Despite the fact that the high dose rate results in faster OSL signal saturation of quartz grains within the ironstones, it allows the dating of young sediments, possibly in a few years age range (<25 years), assuming the estimation of D_e lower than 0.1 Gy and dose rate of 4 Gy/ka.

The unusual dose rates of the Xingu ironstones are related to the high concentrations of ^{238}U and ^{232}Th. The Xingu watershed has headwaters draining sandstones of the Parecis sedimentary basin, but most of the watershed drains granitoid rocks of the Brazilian shield, which host minerals rich both in ^{238}U and ^{232}Th. Typical $^{232}Th/^{238}U$ ratios in most upper crustal rocks are between 3.5 and 4.0, and in sedimentary rocks, $^{232}Th/^{238}U$ values greater than 4.0 may indicate intense weathering in

Table 6
Conventional and calibrated ages and $\delta^{13}C$ of bulk organic matter from selected samples. Ages were calibrated with Calib 7.1 using the SHCal13 calibration curve (Stuiver et al., 2019; Hogg et al., 2020). OSL ages from water saturated (WS) dose rates and exponential (Exp) or exponential plus linear (Exp + lin) dose response curves are showed for comparison. Field codes are presented in Table 2.

Lab code	Lab ID	Conventional age (ka BP)	IRMS $\delta^{13}C$ (‰)	Calibrated age (cal ka BP, 2σ)	WS Exp OSL age (ka)	WS Exp + lin OSL age (ka)
L1244	Beta-533270	20.68 ±- 0.07	−24.1	23.17–22.68	3.4 ± 0.3	3.4 ± 0.4
L1245	Beta-537938	14.22 ± 0.05	−25.9	15.44–15.13	11.3 ± 1.2	13.3 ± 1.8
L1264	Beta-537939	16.10 ± 0.05	−23.6	17.59–17.26	12.8 ± 1.4	14.2 ± 1.6
L1265	Beta-537940	5.59 ± 0.03	−23.7	4.49–4.34	32.5 ± 2.9	33.0 ± 3.1

source areas or sedimentary recycling i.e., derivation from old sedimentary rocks (Asiedu et al., 2000). In most cases, elevation in the $^{232}Th/^{238}U$ ratio is associated to the loss of ^{238}U due to weathering (Asiedu et al., 2000; Pupim et al., 2016). The studied ironstones are composed mainly of quartz sand grains, granules or pebbles immersed in a goethite matrix. In this case, goethite should be the main host of ^{238}U and ^{232}Th. The studied ironstones have $^{232}Th/^{238}U$ ratios with moderate values around 2.2–3.4 to relatively high $^{232}Th/^{238}U$ ratios in the range of 4.5–7.8 (Table 3). The source rocks of sediments supplied to the Xingu River are under heavy and long chemical weathering due low denudation rates in the drainage basin (Wittmann et al., 2010). This could contribute to surface waters and/or fine-grained suspended sediments rich in ^{238}U and ^{232}Th, which are further concentrated by authigenic goethite precipitation as cement of the Xingu River sediments. The variation of $^{232}Th/^{238}U$ ratios also suggests that goethite from ironstones of the Xingu River is precipitated from waters draining source areas with different weathering degree or source rock composition. However, detailed mineral chemistry studies are needed to understand the relatively high concentration of ^{238}U and ^{232}Th in the ironstones and their controlling variables.

The studied ironstones are formed underwater during fluvial sediment deposition followed by goethite precipitation, but experiences seasonal dry phases or long term dry periods due to shifts in the riverbed. Hence, variations in water saturation through play a role for dose rate assessment and should be considered in age uncertainties. The studied samples were water saturated in the laboratory to appraise the maximum range of variation in dose rate. In this way, dose rates were estimated from water saturated and dry samples, showing similar results (Table 5) because of the intense cementation and low porosity of ironstones. Thus, water variation during wet and dry seasons has minor effect on our dating results, assuming that goethite cements are stable after precipitation. However, detailed petrological studies are still needed to evaluate phases of pore filling or generation respectively due to crystallization or dissolution of cements.

5.2. Ironstones ages and formation processes

In this section, we consider a range of OSL ages based on CAM D_e from the medium size aliquots, exponential plus linear dose response function and dose rates from both dry and water saturated samples. In this way, the OSL ages of the studied ironstones ranged from ~60 ka to 3 ka (Table 5). The radiocarbon ages fall in the interval of 17.63–4.46 cal ka BP (Table 6). OSL and radiocarbon ages would indicate the trapping time of detrital quartz and organic matter into the goethite matrix of the ironstones, respectively. Thus, both methods would indicate ironstone formation ages through cementation of terrigenous sediments deposited in the Xingu riverbed. Considering individual samples, we observed a significant age offset between the OSL and radiocarbon ages, which highlight the asynchronous trapping of terrigenous sediments during ironstone formation. As there is no discernible pattern for the offsets, and radiocarbon ages are not systematically younger or older than the OSL ages, it is difficult to hypothesize a specific single cause for the observed difference. Effects related to the OSL ages, pre-aging of organic matter and permeation of young organic carbon into the rock pores could all contribute to this offset. As discussed, processes affecting OSL ages can be related to incomplete bleaching, mixing of grains continuously trapped through time or dose rate microheterogeneities. However, the relatively low overdispersion (<30 %) observed in D_e distributions of some samples would exclude the contribution of both incomplete bleaching, mixing of grains and dose rate microheterogeneities effects. In this case, the high overdispersion of some samples could be attributed to multiple episodes of sediment trapping, thus, suggesting that ironstones growth is a multiphase process. However, a single grain approach coupled with detailed microscopic characterization is recommended to appraise if overdispersion in D_e distributions is related with populations of quartz grains trapped during different phases of ironstones growth.

The organic fraction of the studied ironstones is enriched in ^{13}C ($\delta^{13}C = -25.9$ to -23.6, Table 6) in comparison to organic matter from riverbed sediments ($\delta^{13}C = -31.04$ to -27.49‰) of the lowermost part of the Xingu River (Bertassoli et al., 2017). This could be caused by post-depositional effects (e.g. degradation) and by significantly higher percentages of autochthonous material (e.g., microbial) or C4 plants in the bulk organic matter trapped during the formation of the ironstones. Thus, the organic matter within the ironstones differs from the organic matter of detrital sediments under transport in the Xingu River. The uptake of autochthonous (aquatic) organic matter by ironstones could be favored by the widespread growth of benthic algae over the rocky substrates of the Xingu riverbed (Zualaga-Gómez et al., 2016).

Despite the discussed age uncertainties, the OSL and radiocarbon ages greatly improve our knowledge about the growth timespan of the Xingu ironstones. According to the obtained OSL and radiocarbon ages, the ironstones of the Xingu River are younger than goethite crusts found in upland terrains from Amazonia (e.g., Allard et al., 2018) or in other regions in Brazil (Riffel et al., 2016), which should have an origin related to tropical soil development. The studied ironstones are restricted to the Xingu River channel, in areas permanently or seasonally inundated and with lotic water conditions. This environment somehow promotes conditions suitable for authigenic goethite crystallization and cementation of terrigenous sediments transported by the Xingu River. The OSL ages suggest that this system has been functioning for a thousand years, at least since the late Pleistocene, creating specific habitats for the aquatic biota adapted to turbulent flows in clear water Amazonian rivers (Zuluaga-Gómez et al., 2016). However, we highlight that the presented OSL and radiocarbon ages should represent minimum ages for the Xingu ironstone system because our sampling was restricted to the uppermost layer of ironstones lying over the riverbed as well as because of the low preservation potential of ironstones in the long term due the high erosion capacity of the Xingu rapids. The climate and geochemical controls on this system is still unknown, but the OSL ages give the first timescale to shed light on formation processes of the Xingu ironstones.

6. Conclusions

This is the first application of quartz OSL dating to Quaternary ironstones. However, the high dose rates observed in the studied goethite-cemented ironstones limit the quartz OSL dating to around 71 ka. For some studied samples, D_e distributions with low OD suggest grains that quartz grains are well bleached prior to deposition while samples with D_e distributions showing high OD are attributed to the presence of quartz grains populations trapped through time.

The $^{232}Th/^{238}U$ ratio values indicate that most of the studied ironstones comprise sediments sourced from rocks under intense weathering

conditions. The OSL ages are between ~60 ka and 3 ka, indicating a Late Pleistocene and Holocene system responsible for ironstone formation in the Xingu River. The OSL ages improve the understanding of the genesis of ironstones, suggesting they are related with the Quaternary hydrology of the Xingu River. Future luminescence dating studies are recommended to extend the age limit and establish a regional chronological framework of the Xingu River ironstones in order to achieve a better understanding of their geochemical and/or hydrological controls.

Declaration of competing interest

The authors declare that they have no known competing financial interests or personal relationships that could have appeared to influence the work reported in this paper.

Acknowledgments

We are grateful to the anonymous reviewers and Editor Frank Preusser for the critical and careful comments, which decisively improved the quality of our manuscript. This research was supported by São Paulo Research Foundation (FAPESP grants 2016/02656-9 and 2018/23899-2). AOS and FNP are funded by Conselho Nacional de Desenvolvimento Científico e Tecnológico (CNPq grants 304727/2017-2 and #302411/2018-6). DJB was supported by FAPESP (grants 2016/11141-2, 2018/15123-4, 2019/24349-9 and 2019/24977-0). PN is grateful to National Council for Science and Technology Development (CNPq), The World Academy of Sciences (TWAS) (CNPq/TWAS grant 154507/2017-2) and The São Paulo Research Foundation (FAPESP grant 2019/04059-6) for funding his PhD fellowship at the University of São Paulo. FCGR is grateful to FAPESP for funding her PhD fellowship at the University of São Paulo (FAPESP grant 2018/12472-8). We would like to thank Thays Desirée Mineli and Ian del Río for their assistance during luminescence measurements and data analysis.

References

Allard, T., Gautheron, C., Riffel, S.B., Balan, E., Soares, B.F., Pinna-Jamme, R., Derycke, A., Morin, G., Bueno, G.T., do Nascimento, N., 2018. Combined dating of goethites and kaolinites from ferruginous duricrusts. Deciphering the Late Neogene erosion history of Central Amazonia. Chem. Geol. 479, 136–150.

Arnold, L.J., Bailey, R.M., Tucker, G.E., 2007. Statistical treatment of fluvial dose distributions from southern Colorado arroyo deposits. Quat. Geochronol. 2, 162–167.

Arnold, L.J., Roberts, R.G., 2009. Stochastic modeling of multi-grain equivalent dose (D_e) distributions: implications for OSL dating of sediment mixtures. Quat. Geochronol. 4, 204–230.

Asiedu, D.K., Suzuki, S., Nogami, K., Shibata, T., 2000. Geochemistry of lower cretaceous sediments, inner zone of southwest Japan. Constraints on provenance and tectonic environment. Geochem. J. 34, 155–173.

Bahia, R.B.C., Faraco, M.T.L., Monteiro, M.A.S., Oliveira, M.A.O., 2004. Folha SA.22-Belém. In: Schobbenhaus, C., Gonçalves, J.H., Santos, J.O.S., Abram, M.B., Leão Neto, R., Matos, G.M.M., Vidotti, R.M., Ramos, M.A.B., Jesus, J.D.A.de (Eds.), Carta Geológica do Brasil ao Milionésimo. Sistema de Informações Geográficas. Programa Geologia do Brasil. CPRM, Brasilia, CD-ROM.

Bertassoli Jr., D.J., Sawakuchi, A.O., Chiessi, C.M., Schefuβ, E., Hartmann, G.A., Häggi, C., Cruz, F.W., Zabel, M., McGlue, M., Santos, R.A., Pupim, F.N., 2019. Spatiotemporal variations of riverine discharge within the Amazon basin during the Late Holocene coincide with extratropical temperature anomalies. Geophys. Res. Lett. 46 (15), 9013–9022.

Bertassoli Jr., D.J., Sawakuchi, A.O., Sawakuchi, H.O., Pupim, F.N., Hartmann, G.A., McGlue, M.M., Chiessi, C.M., Zabel, M., Schefuß, E., Pereira, T.S., Santos, R.A., Faustino, S.B., Oliveira, P.E., Bicudo, D.C., 2017. The fate of carbon in sediments of the Xingu and Tapajós clearwater rivers, Eastern Amazon. Front. Mar. Sci. 4 https://doi.org/10.3389/fmars.2017.00044.

Bøtter-Jensen, L., Bulur, E., Duller, G.A.T., Murray, A.S., 2000. Advances in luminescence instrument systems. Radiat. Meas. 32, 523–528.

David, B., Roberts, R.G., Magee, J., Mialanes, J., Turney, C., Bird, M., White, C., Fifield, L.K., Tibby, J., 2007. Sediment mixing at Nonda Rock: investigations of stratigraphic integrity at an early archaeological site in northern Australia and implications for the human colonisation of the continent. J. Quat. Sci. 22, 449–479.

Duller, G.A.T., 2003. Distinguishing quartz and feldspar in single grain luminescence measurements. Radiat. Meas. 37, 161–165.

Duller, G.A.T., 2015. The Analyst software package for luminescence data: overview and recent improvements. Ancient TL 33, 35–42.

Filizola, N.P., 1999. In: O fluxo de sedimentos em suspensão nos rios da bacia Amazônica Brasileira. Publicação ANEEL, Brasília, p. 63.

Fitzgerald, D.B., Sabaj Perez, M.H., Sousa, L.M., Gonçalves, A.P., Rapp Py-Daniel, L., Lujan, N.K., Zuanon, J., Winemiller, K.O., Lundberg, J.G., 2018. Diversity and community structure of rapids-dwelling fishes of the Xingu River: implications for conservation amid large-scale hydroelectric development. Biol. Conserv. 222, 104–112.

Galbraith, R.F., Roberts, R.G., Laslett, G.M., Yoshida, H., Olley, J.M., 1999. Optical dating of single and multiple grains of quartz from Jinmium rock shelter, Northern Australia: part I, experimental design and statistical models. Archaeometry 41, 339–364.

Giral-Kacmarkcik, S., Savin, S.M., Nahon, D., Girard, J.-P., Lucas, Y., Abel, L., 1998. Oxygen isotope geochemistry of kaolinite in laterite-forming processes, Manaus, Amazonas, Brazil. Geochem. Cosmochim. Acta 62, 1865–1879.

Girard, J.P., Freyssinet, P., Morillon, A.C., 2002. Oxygen isotope study of Cayenne duricrust paleosurfaces: implications for past climate and laterization processes over French Guiana. Chem. Geol. 191, 329–343.

Girard, J.-P., Freyssinet, P., Chazot, G., 2000. Unraveling climatic changes from intraprofile variation in oxygen and hydrogen isotopic composition of goethite and kaolinite in laterites: an integrated study from Yaou, French Guiana. Geochem. Cosmochim. Acta 64 (3), 409–426.

Guedes, C.C.F., Sawakuchi, A.O., Giannini, P.C.F., DeWitt, R., Aguiar, V.A.P., 2013. Luminescence characteristics of quartz from Brazilian sediments and constraints for OSL dating. An Acad. Bras Ciências 85, 1303–1316.

Guerin, G., Mercier, N., Adamiec, G., 2011. Dose-rate conversion factors: update. Ancient TL 29, 5–8.

Hogg, A.G., Heaton, T.J., Hua, Q., Palmer, J.G., Turney, C.S.M., Southon, J., Bayliss, A., Blackwell, P.G., Boswijk, G., Ramsey, C.B., Pearson, C., Petchey, F., Reimer, P., Reimer, R., Wacker, L., 2020. SHCal20 Southern hemisphere calibration, 0–55,000 years Cal BP. Radiocarbon 62 (4), 759–778.

Jacobs, Z., Roberts, R.G., 2007. Advances in optically stimulated luminescence dating of individual grains of quartz from archeological deposits. Evol. Anthropol. 16, 210–223.

Kreutzer, S., Schmidt, C., Fuchs, M.C., Dietze, M., Fischer, M., Fuchs, M., 2012. Introducing an R package for luminescence dating analysis. Ancient TL 30, 1–8.

Marengo, J.A., 2004. Interdecadal variability and trends of rainfall across the Amazon basin. Theor. Appl. Climatol. 78, 79–96.

Meade, R.H., Rayol, J.M., Conceição, S.C., Natividade, J.R.G., 1991. Backwater effects in the Amazon river basin of Brazil. Environ. Geol. Water Sci. 18, 105–114.

Mejdahl, V., Christiansen, H.H., 1994. Procedures used for luminescence dating of sediments. Quat. Sci. Rev. 13, 403–406.

Mineli, T.D., Sawakuchi, A.O., Guralnik, B., Lambert, R., Jain, M., Pupim, F.N., del Río, I. A.G., Nogueira, L., 2021. Variation of luminescence sensitivity, characteristic dose and trap parameters of quartz from rocks and sediments. Radiat. Meas. 144, 106583.

Murray, A.S., Wintle, A.G., 2000. Luminescence dating of quartz using an improved single-aliquot regenerative-dose protocol. Radiat. Meas. 32, 57–73.

Murray, A.S., Wintle, A.G., 2003. The single aliquot regenerative dose protocol: potential for improvements in reliability. Radiat. Meas. 37 (4–5), 377–381.

Nathan, R.P., Thomas, P.J., Jain, M., Murray, A.S., Rhodes, E.J., 2003. Environmental dose rate heterogeneity of beta radiation and its implications for luminescence dating: Monte Carlo modelling experimental validation. Radiat. Meas. 37, 305–313.

Nogueira, C., Buckup, P.A., Menezes, N.A., Oyakawa, O.T., Kasecker, T.P., Neto, M.B.R., da Silva, J.M.C., 2010. Restricted-range fishes and the conservation of Brazilian freshwaters. PLoS One 5 (6), 1–10.

Prescott, J.R., Hutton, J.T., 1994. Cosmic ray contributions to dose rates for luminescence and ESR dating: large depths and long-term time variations. Radiat. Meas. 23, 497–500.

Pupim, F.N., Bierman, P.R., Assine, M.L., Rood, D.H., Silva, A., Merino, E.R., 2015. Erosion rates and landscape evolution of the lowlands of the Upper Paraguay River basin (Brazil) from cosmogenic ^{10}Be. Geomorphology 234, 151–160.

Pupim, F.N., Sawakuchi, A.O., Almeida, R.P., Ribas, C.C., Kern, A.K., Hartmann, G.A., Chiessi, C.M., Tamura, L.N., Mineli, T.D., Savian, J.F., Grohmann, C.H., Bertassoli Jr., D.J., Stern, A.G., Cruz, F.W., Cracraft, J., 2019. Chronology of Terra Firme formation in Amazonian lowlands reveals a dynamic Quaternary landscape. Quat. Sci. Rev. 210, 154–163.

Pupim, F.N., Sawakuchi, A.O., Mineli, T.D., Nogueira, L., 2016. Evaluating isothermal thermoluminescence and thermally transferred optically stimulated luminescence for dating of Pleistocene sediments in Amazonia. Quat. Geochronol. 36, 28–37.

Ribeiro, L.M.A.L., Sawakuchi, A.O., Wang, H., Sallun Filho, W., Nogueira, L., 2015. OSL dating of Brazilian fluvial carbonates (tufas) using detrital quartz grains. Quat. Int. 362, 146–156.

Riffel, S.B., Vasconcelos, P.M., Carmo, I.O., Farley, K.A., 2016. Goethite (U–Th)/He geochronology and precipitation mechanisms during weathering of basalts. Chem. Geol. 446, 18–32.

Rodnight, H., Duller, G.A.T., Tooth, S., Wintle, A.G., 2005. Optical dating of a scroll-bar sequence on the Klip River, South Africa, to derive the lateral migration rate of a meander bend. Holocene 15, 802–811.

Sawakuchi, A.O., Hartmann, G.A., Sawakuchi, H.O., Pupim, F.N., Bertassoli Jr., D.J., Parra, M., Antinao, J.L., Sousa, L.M., Sabaj Perez, M.H., Oliveira, P.E., Santos, R.A., Savian, J.F., Grohmann, C.H., Medeiros, V.B., McGlue, M.M., Bicudo, D.C., Faustino, S.B., 2015. The Volta Grande do Xingu: reconstruction of past environments and forecasting of future scenarios of a unique Amazonian fluvial landscape. Sci. Drill. 20, 21–32.

Sawakuchi, A.O., Kalchgruber, R., Giannini, P.C.F., Nascimento Jr., D.R., Guedes, C.C.F., Umisedo, N.K., 2008. The development of blowouts and foredunes in the Ilha

Comprida barrier (Southeastern Brazil): the influence of Late Holocene climate changes on coastal sedimentation. Quat. Sci. Rev. 27, 2076–2090.
Sawakuchi, A.O., Mendes, V.R., Pupim, F.N., Mineli, T.D., Ribeiro, L.M.A.L., Zular, A., Guedes, C.C.F., Giannini, P.C.F., Nogueira, L., Sallun Filho, W., Assine, M.L., 2016. Optically stimulated luminescence and isothermal thermoluminescence dating of high sensitivity and well bleached quartz from Brazilian sediments: from Late Holocene to beyond the Quaternary? Braz. J. Genet. 46 (1), 209–226.
Sioli, H., 1984. In: The Amazon: Limnology and Landscape Ecology of a Mighty Tropical River and its Basin. Kluwer Academic Publishers, Dordrecht, Boston.
Soares, E.A.A., Tatumi, S.H., Riccomini, C., 2010. OSL age determination of Pleistocene fluvial deposits in Central Amazonia. An Acad. Bras Ciências 82, 691–699.
Stuiver, M., Reimer, P.J., Reimer, R.W., 2019. CALIB 7.1 [WWW program] at. http://calib.org. (Accessed 18 December 2019).
Timar-Gabor, A., Vasiliniuc, S., Vandenberghe, D.A.G., Cosma, C., Wintle, A.G., 2012. Investigations into the reliability of SAR-OSL equivalent doses obtained for quartz samples displaying dose response curves with more than one component. Radiat. Meas. 47, 740–745.
Tsakalos, V., Dimitriou, E., Kazantzaki, M., Anagnostou, C., Christodoulakis, J., Filippaki, E., 2018. Testing optically stimulated luminescence dating on sand-sized quartz of deltaic deposits from the Sperchios delta plain, central Greece. J. Palaeogeogr. 7, 130–145.
Wallinga, J., 2002. On the detection of OSL age overestimation using single-aliquot techniques. Geochronometria 21, 17–26.
Wintle, A.G., Murray, A.S., 2006. A review of quartz optically stimulated luminescence characteristics and their relevance in single aliquot regeneration dating protocols. Radiat. Meas. 41, 369–391.
Wittmann, H., von Blanckenburg, F., Maurice, L., Guyot, L., Filizola, N., Kubik, P.W., 2010. Sediment production and delivery in the Amazon River basin quantified by in situ-produced cosmogenic nuclides and recent river loads. Geol. Soc. Am. Bull., B30317, 1.
Zuluaga-Gómez, M.A., Fitzgerald, D.B., Giarrizzo, T., Winemiller, K.O., 2016. Morphologic and trophic diversity of fish assemblages in rapids of the Xingu River, a major Amazon tributary and region of endemism. Environ. Biol. Fish. 99, 647–658.